Supplement of Atmos. Chem. Phys., 26, 1889–1906, 2026
https://doi.org/10.5194/acp-26-1889-2026-supplement

Atmospheric Chemistry and Physics
Open Access
EGU

Supplement of

Why observed and modelled ozone production rates and sensitives differ, a case study at rural site in China

Jun Zhou et al.

Correspondence to: Jun Zhou (junzhou@jnu.edu.cn) and Min Shao (mshao@jnu.edu.cn)

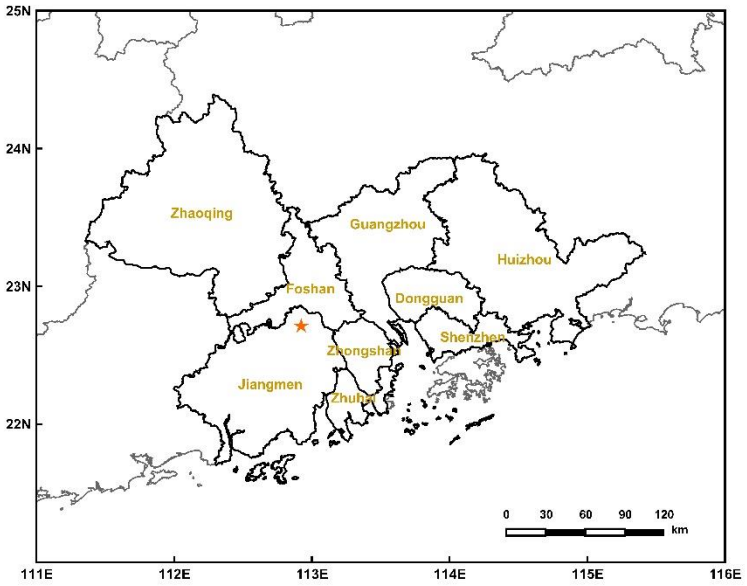

Figure S1: Map of the Pearl River Delta showing the location of the Guangdong Atmospheric Supersite of China (112.93°E, 22.73°N). Created using MeteoInfo v3.6.2.

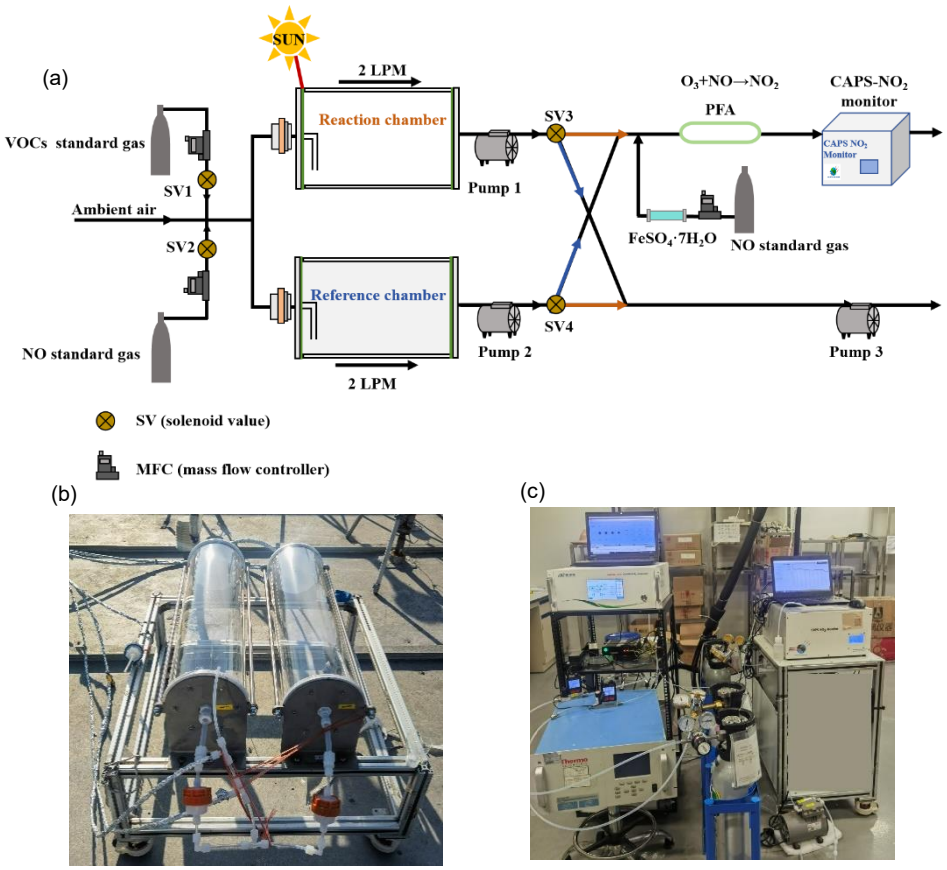

Figure S2: Schematic (a) and actual image (b–c) of the NPOPR detection system; (b) outdoor section of the NPOPR detection system; (c) indoor section of the NPOPR detection system.

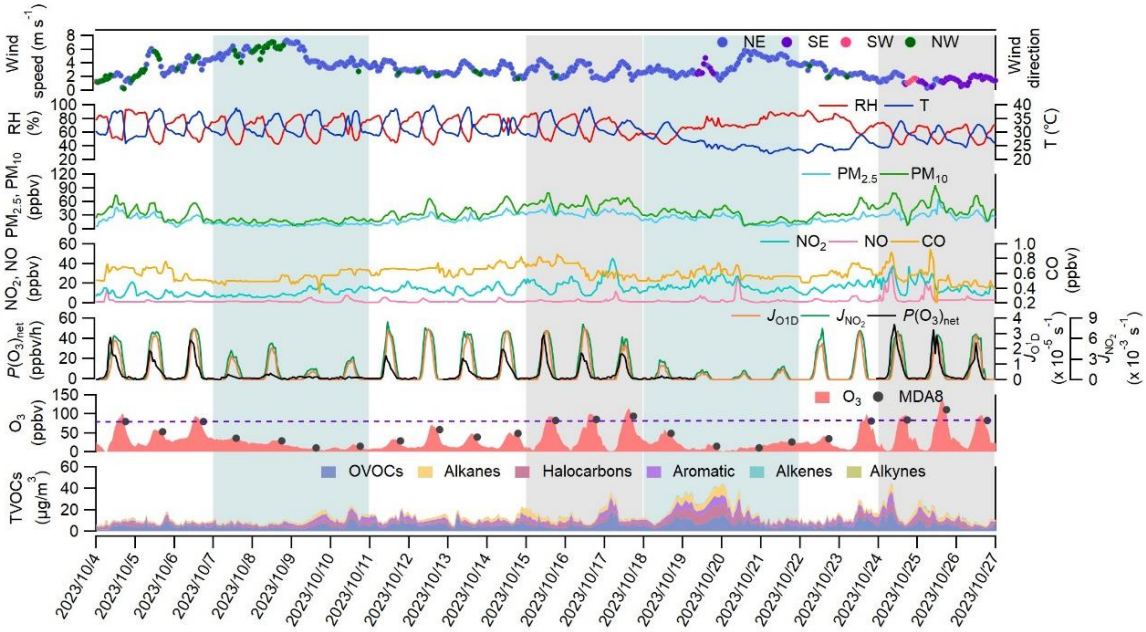

Figure S3: The time series of ozone, its precursors, meteorological parameters, and $P(O_3)_{net}$_Mea (measured $P(O_3)_{net}$) at Guangdong Atmospheric Supersite of China from October 4 to October 20, 2023). The blue and gray shaded areas represent rainy days and O_3 pollution days, respectively.

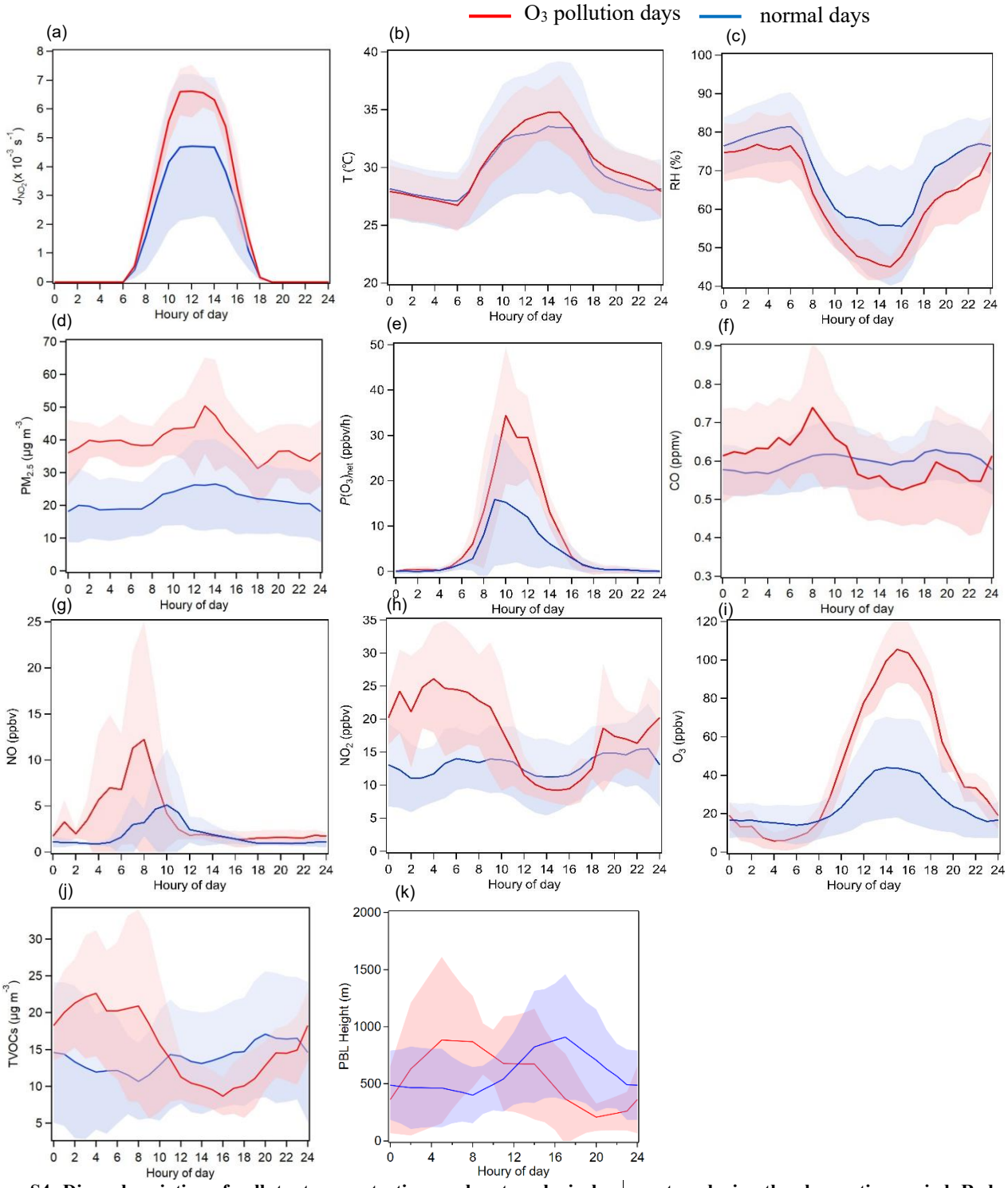

Figure S4: Diurnal variation of pollutant concentrations and meteorological parameters during the observation period. Red solid line: O_3 pollution days; blue solid line: normal days.

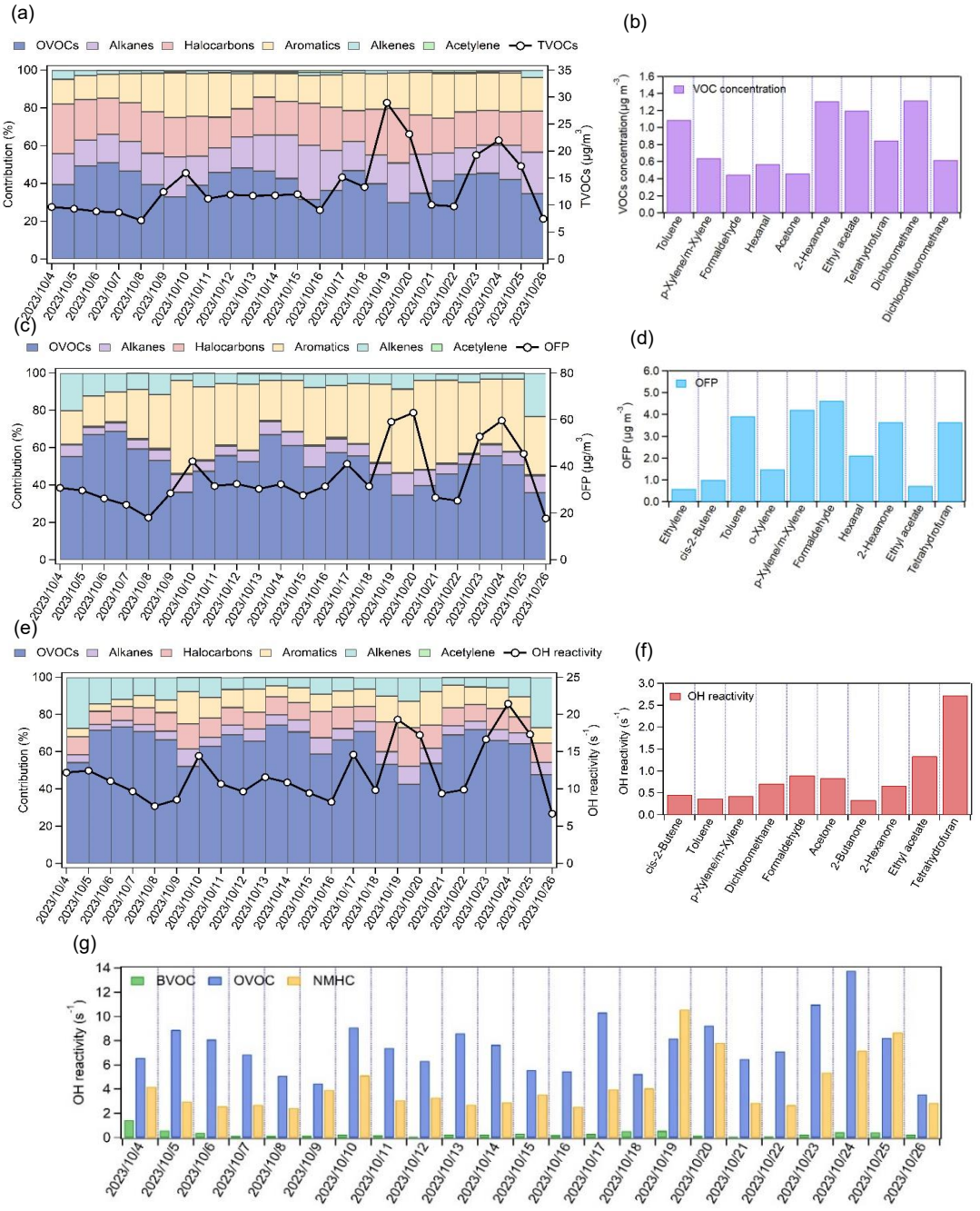

Figure S5: Daily contributions of VOC categories (OVOCs, alkanes, halocarbons, aromatics, alkenes, and alkynes) to (a) VOCs concentration, (b) total OH reactivity (k_{OH}), and (c) O_3 formation potential (OFP) during the observation period. (d), (e), and (f) represent the top 10 contributing species for VOCs concentration, k_{OH}, and OFP, respectively. (g) daytime average concentration of different VOC categories (BVOCs, OVOCs, and NMHC) during the observation period.

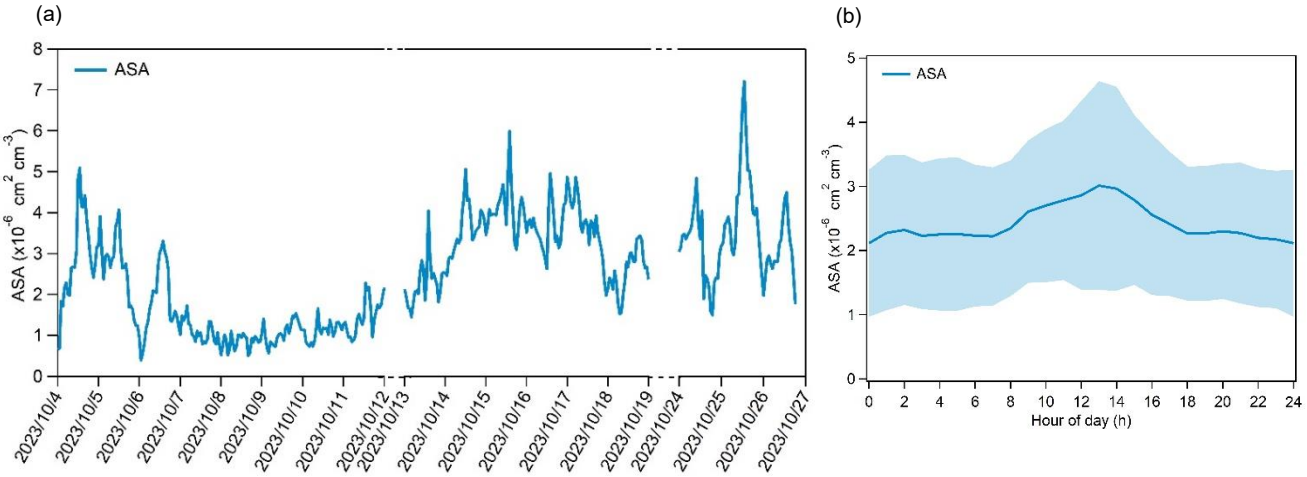

Figure S6: (a) Time series and (b) diurnal variation of aerosol surface area during the observation period.

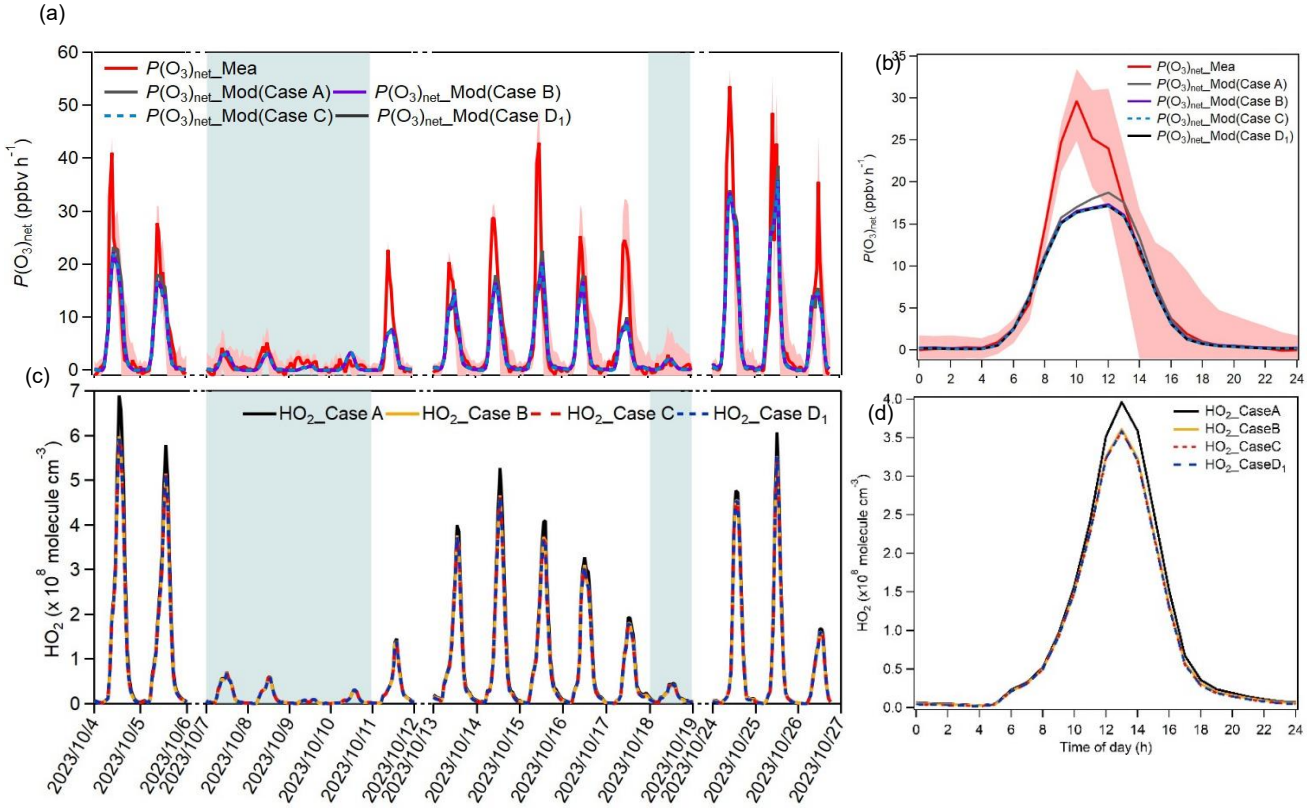

Figure S7: Time series and diurnal variations of (a)–(b) $P(O_3)_{net}$ (Case A–D_1) and (c)-(d) HO_2 (Case A–D_1) during the observation period. The diurnal variations were calculated by excluding rainy days, which are marked as the shaded areas in (a) and (c)).

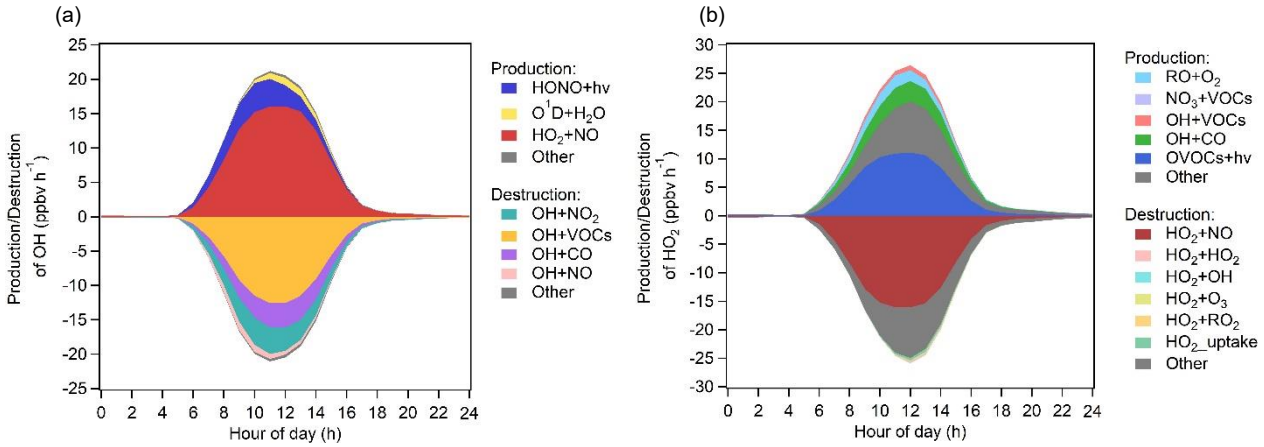

Figure S8: The chemical budget of (a) OH and (b) HO_2 simulated in Case D_1.

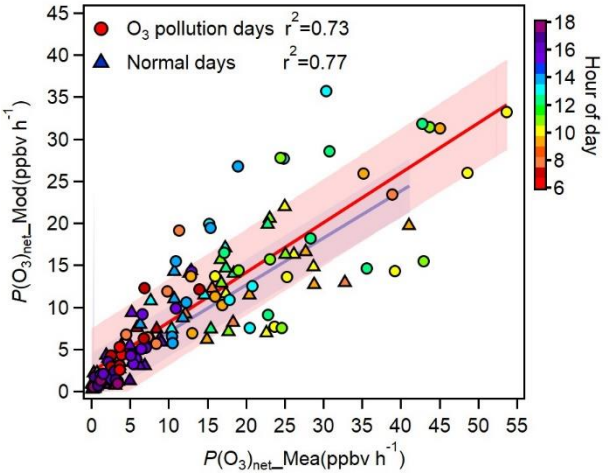

Figure S9. Correlations between simulated ($P(O_3)_{net}$_Mod) and measured ($P(O_3)_{net}$_Mea) $P(O_3)_{net}$ on O_3 pollution days and normal days.

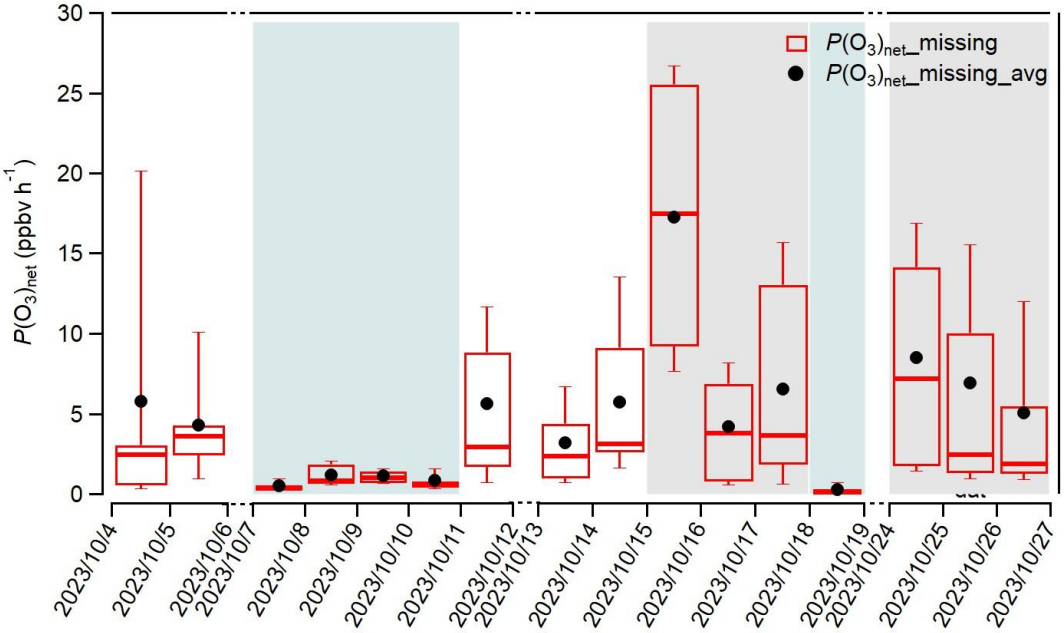

Figure S10: Box plots of $P(O_3)_{net}$_missing (Case D_1) on each day during the observation period. The box boundaries represent the 10th and 90th percentiles; the midline indicates the 50th percentile, and the black dots denote the daily average values of $P(O_3)_{net}$_missing. The blue and gray shaded areas represent rainy days and O_3 pollution days, respectively.

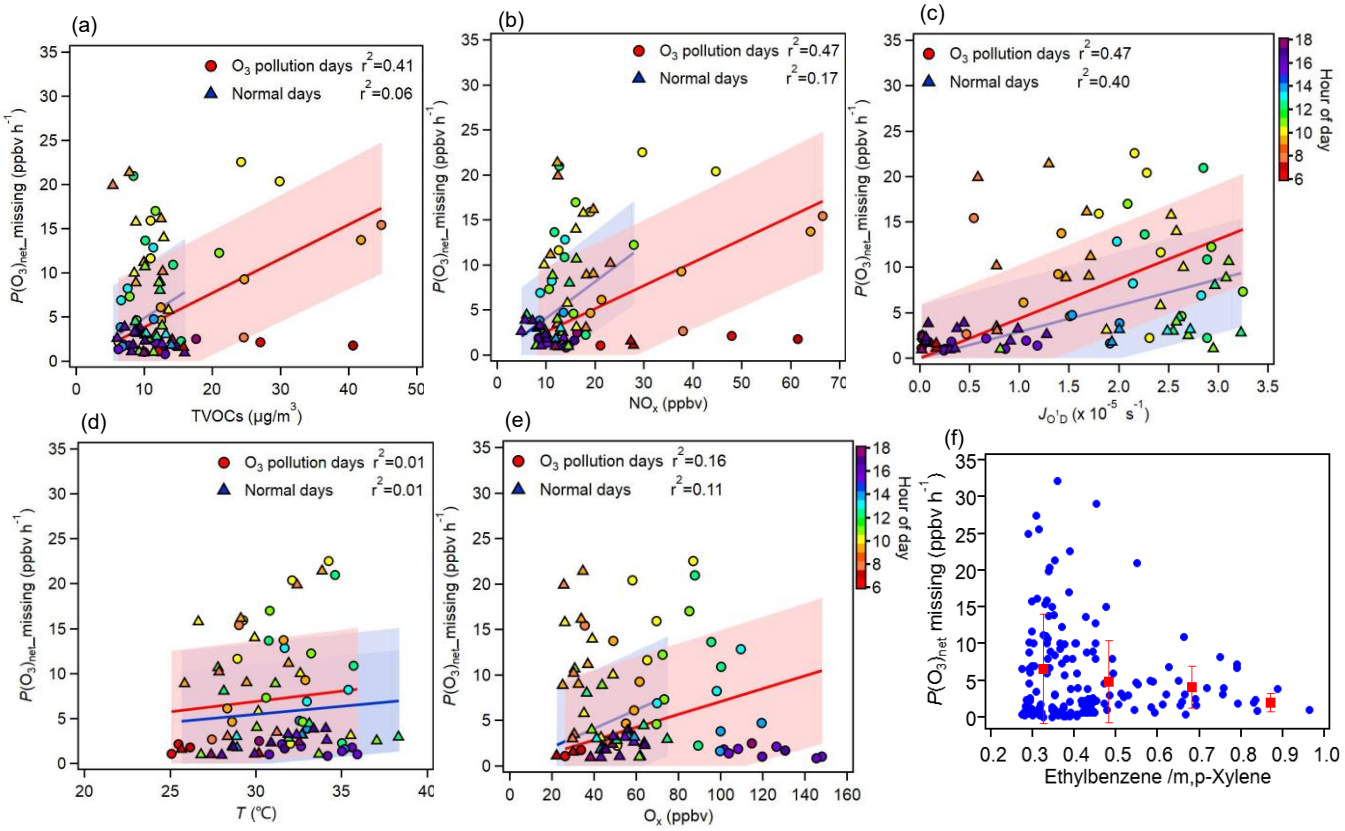

Figure S11: Correlations between $P(O_3)_{net}$_missing and TVOCs, NOx, J_{O1D}, *T*, Ox (a–e), and the ethylbenzene/m,p-Xylene ratio (f, representing the air mass aging). Circles represent O_3 pollution days, triangles represent normal days, and the shaded area indicates the 68.3 % confidence interval of the fitting line.

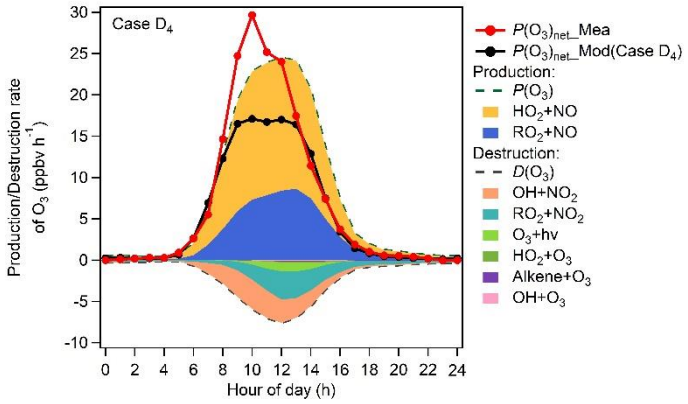

Figure S12: Diurnal variations of measured $P(O_3)_{net}$ values, simulated values under Case D_4 scenario, and different pathways of O_3 production and destruction. Diurnal variations were calculated by excluding rainy days.

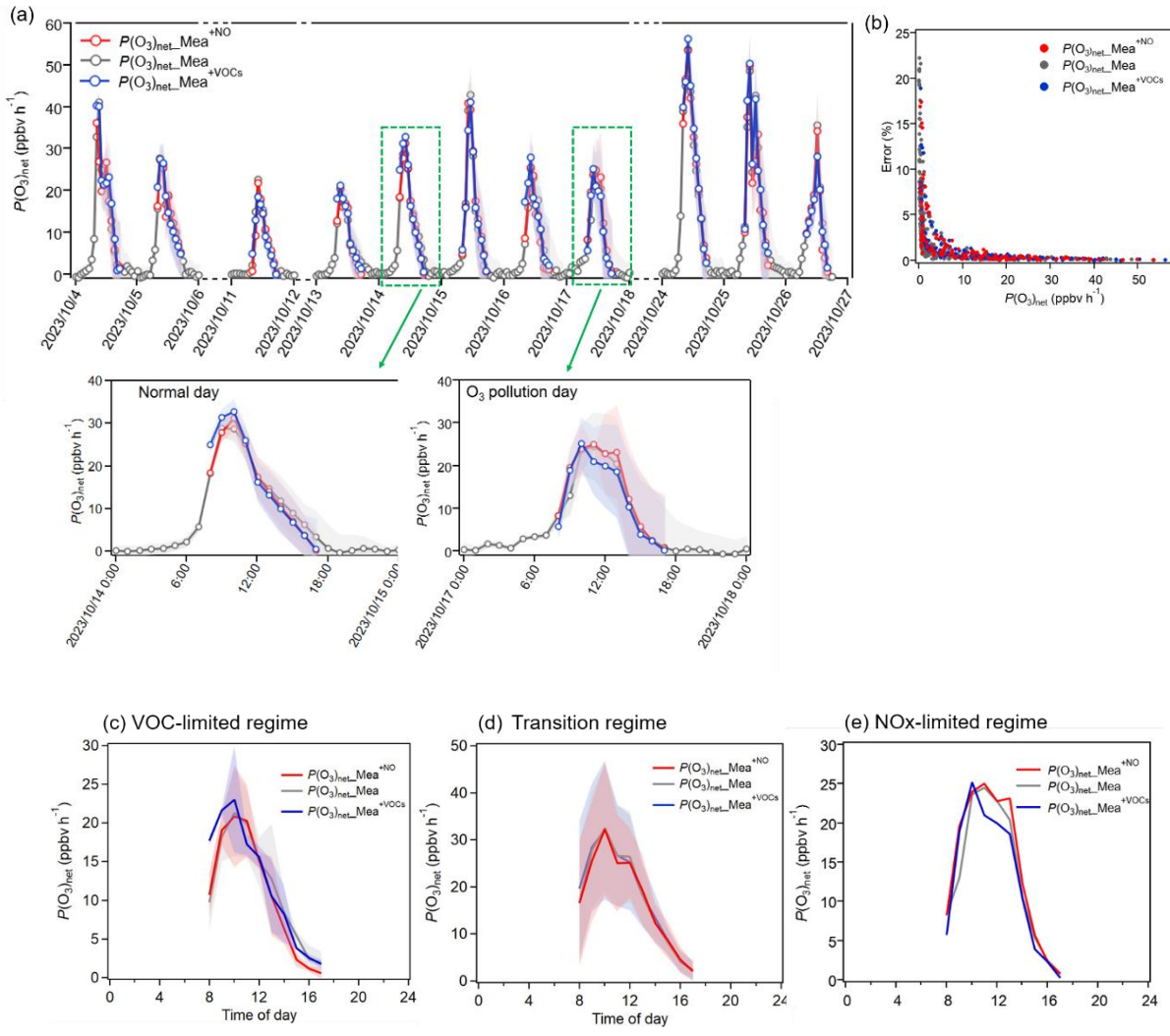

Figure S13: (a) Time series of measured $P(O_3)_{net}$_Mea, $P(O_3)_{net}^{+NO}$ and $P(O_3)_{net}^{+VOCs}$ based on sensitivity experiments using the NPOPR detection system, with an enlarged view for an O_3 pollution day (October 26, 2023) and a normal (O_3 non-pollution) day (October 14, 2023). The shaded areas represent the errors of each measured term, calculated from the instrument measurement uncertainties given in Hao et al. (2023); (b) Relative errors of measured $P(O_3)_{net}$_Mea, $P(O_3)_{net}^{+NO}$, and $P(O_3)_{net}^{+VOCs}$ as a function of their measured values; (c-e) Mean diurnal profiles of the three O_3 formation regimes identified: eight days classified as transition regime (4-5, 11, 14-15, 24-26 October 2023, two as VOC-limited regime (13 and 16 October 2023), and one as NOx-limited regime (17 October 2023).

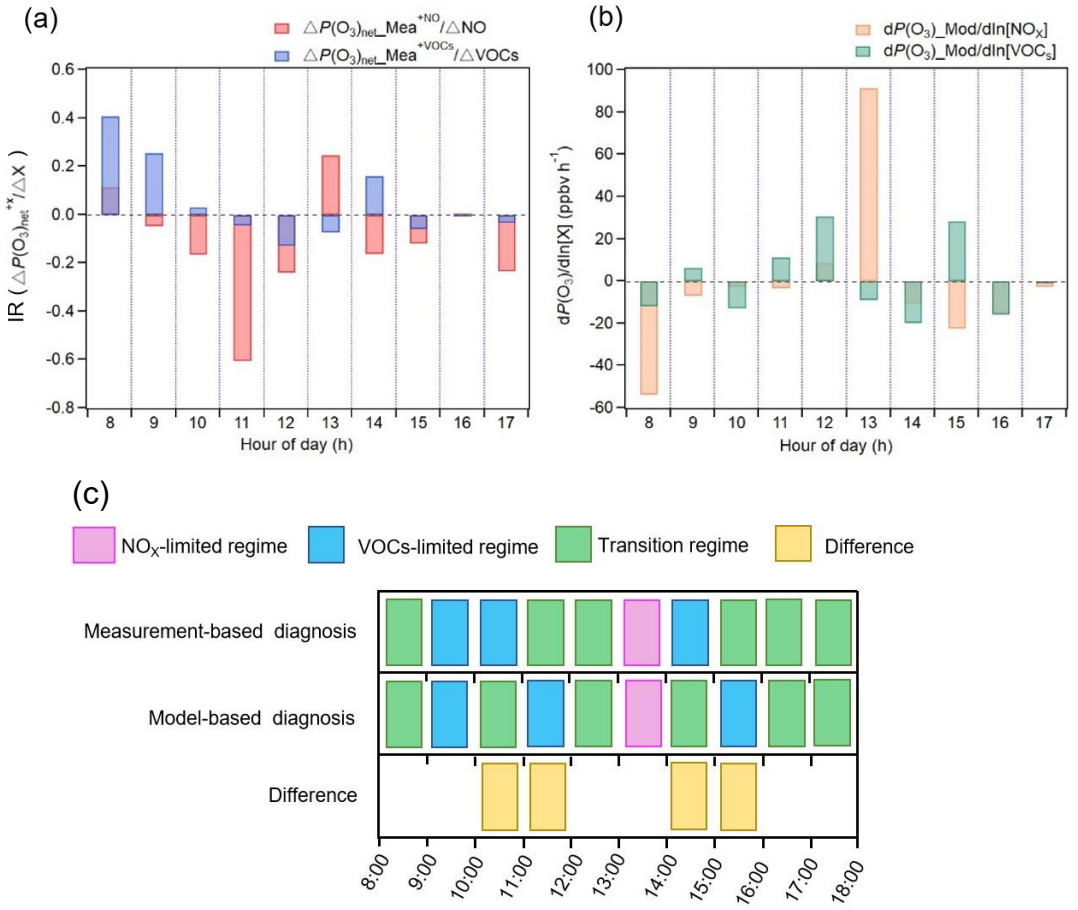

Figure S14: Diurnal variations of $P(O_3)_{net}$ and OFS diagnosis results. (a) direct measurement IR indices ($\Delta P(O_3)_{net}^{+NO}$ and $\Delta P(O_3)_{net}^{+VOCs}$ measured by the NPOPR detection system); (b) absolute $P(O_3)_{net}$ sensitivity of NO_X and VOCs calculated based on the OBM model (Case D_1); (c) OFS diagnosis results and differences between direct measurements (a) and model simulations (b).

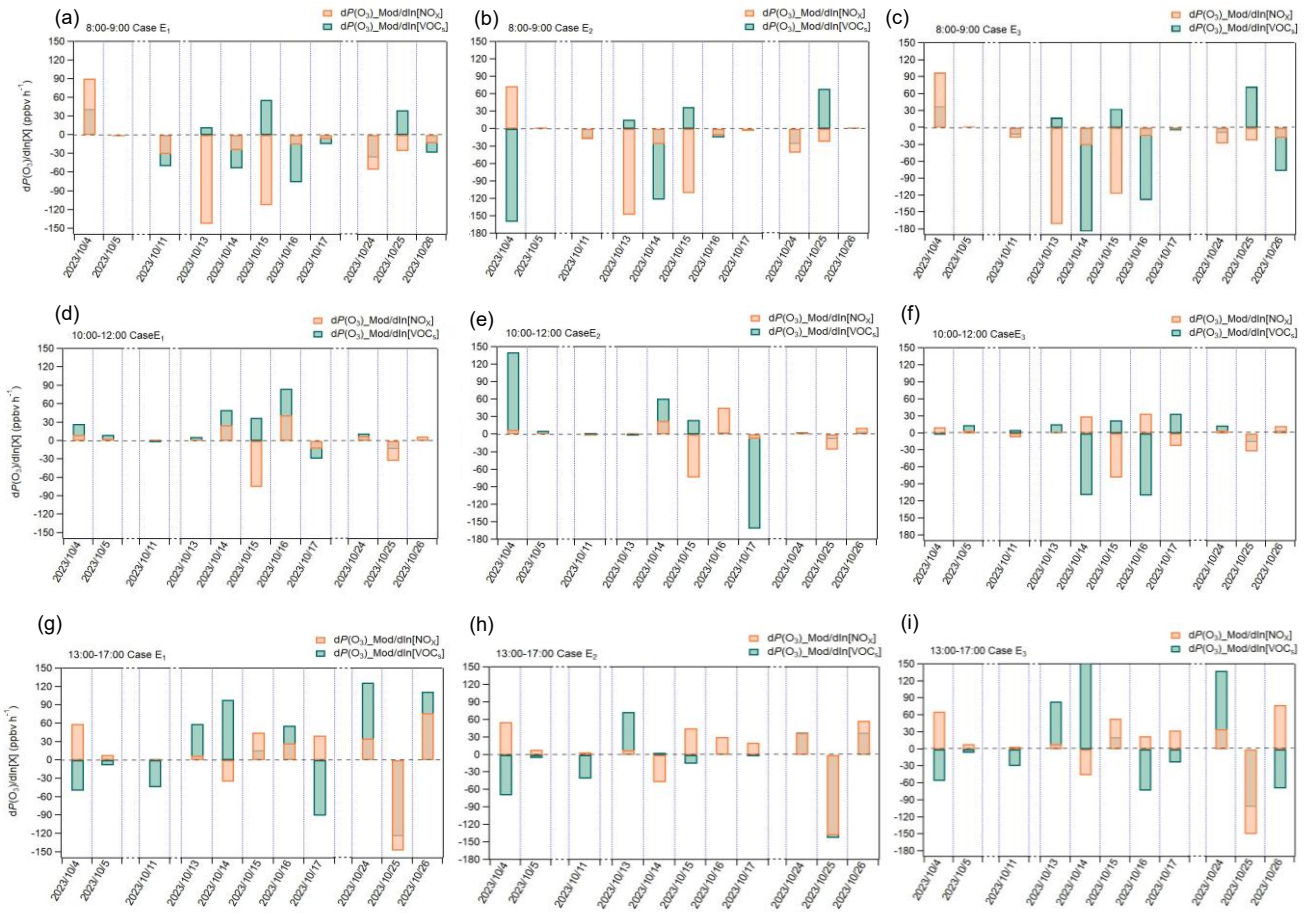

Figure S15: Diurnal cumulative average results of the absolute $P(O_3)_{net}$ sensitivity calculated from the box model (Case E_1–E_3). (a)–(c) $P(O_3)_{net}$ rising phase (8:00–9:00); (d)–(f) $P(O_3)_{net}$ stable phase (10:00–12:00); (g)–(i) $P(O_3)_{net}$ declining phase (13:00–17:00).

S1. Measurement error of $P(O_3)_{net}$ of the NPOPR detection system

We have thoroughly described the measurement error of $P(O_3)_{net}$ of the NPOPR detection system in our previous study (Hao et al., 2023; Zhou et al., 2024b). The measurement error of $P(O_3)_{net}$ depends on the estimation error of Ox in the reaction and reference chambers, which includes the measurement error of O_X of CAPS-NO_2 monitor and the error caused by the light-enhanced loss coefficient of O_3 (γ), which can be calculated as follows:

$$(O_X)_{error} = \sqrt{(O_{X_\gamma})_{error}^{2} + (O_{X_{CAPS}})_{error}^{2}} \quad (S1)$$

where $(O_X)_{error}$ represents the absolute error in the estimated O_X concentration in the reaction and reference chambers, which results from the quadratic propogation of the absolute errors $(O_{X_\gamma})_{error}$ and $(O_{X_{CAPS}})_{error}$. Here, $(O_{X_{CAPS}})_{error}$ signifies the measurement error of the O_X measured by the CAPS-NO_2 monitor, while $(O_{X_\gamma})_{error}$ denotes the error associated with the γ-corrected Ox of the chambers, where γ represent the light-enhanced O_3 loss coefficient.

To get $(O_{X_{CAPS}})_{error}$, we calibrated the CAPS-NO_2 monitor as follows: a. injected ~10–100 ppbv of NO_2 for 30 minutes to passivate the surfaces of the monitor and then injecting ultrapure air for ~ 10 minutes to ensure the zero point did not drift, according to the ultrapure air condition, the LOD of CAPS was 0.88 and 0.02 ppbv (3 σ) at an integration time of 35 and 100 s, respectively; b. injected a wide range of NO_2 concentration (from 0–160 ppbv) prepared from a NO_2 standard gas (with the original concentration of 2.08 ppmv) mixed with ultrapure air into the CAPS-NO_2 monitor, repeated the experiments for three times at each NO_2 concentration, the final results are shown in Fig. S16.

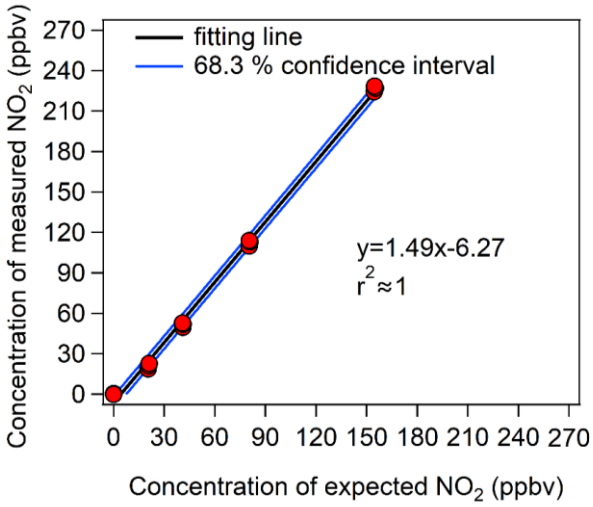

Figure S16: Calibration results of the CAPS NO_2 monitor at different NO_2 mixing ratios. The y-axis represents the NO_2 mixing ratios measured by the CAPS NO_2 monitor, and the x-axis represents the prepared NO_2 mixing ratios prepared from the diluted NO_2 standard gas.

We fitted the calibration results with a 68.3 % confidence level, and the blue line in Fig. S16 represents the maximum fluctuation range under this confidence level, $(O_{X_{CAPS}})_{error}$ was then calculated from the fluctuation range of the 68.3 % confidence interval of the calibration curve, the relationship between the $(O_{X_{CAPS}})_{error}$ and the measured Ox value ($[Ox]_{measured}$)

can be expressed as a power function curve, as shown in Eq. (S2) :

$$(O_{X_{CAPS}})_{error} = 9.72 \times [0x]_{measured}^{-1.0024} \quad (S2)$$

We acknowledge that this power function has been derived from calibration data of the O_X concentrations ranged from 20 ppbv to 160 ppbv. Utilizing this function outside this calibrated range, especially at very low O_X concentrations, may result in errors that are disproportionately large and may not accurately capture the true variability of the measurement errors. In this study, the O_X concentrations ranged from 18 to 148 ppbv, which falls into the calibration range. Consequently, this power function is deemed appropriate for estimating the $(O_{X_{CAPS}})_{error}$ throughout the whole measurement period.

$(O_{X_\gamma})_{error}$ was derived from the light-enhanced loss of O_3 in the reaction and reference chambers at 2.1 L min^{-1}, the flow rate used during the observation campaign. To establish the calibration curve, we performed an outdoor experiment: O_3 (~ 130 ppbv), produced by an O_3 generator (P/N 97-0067-02, Analytic Jena US, USA), was induced into the two chambers. Zero air was co-injected with the O_3 to suppress any photochemical O_3 production outdoors. This setup allowed us to monitor daytime changes in the photolysis frequencies of various species. We simultaneously recorded $J(O^1D)$, T, RH, P and O_3 mixing ratios at the inlets and outlets of both chambers. T and RH were measured with a thermometer (Vaisala, HMP110, USA). The light-enhanced O_3 loss coefficient (γ) was then calculated using Eq. (S3):

$$\gamma = \frac{d[O_3] \times D}{\omega \times [O_3] \times \tau} \quad (S3)$$

where $d[O_3]$ represents the difference between the O_3 mixing ratios at the inlets and outlets of both chambers (i.e., the light-enhanced O_3 loss); D is the diameter of the chambers; ω is the average velocity of O_3 molecules; $[O_3]$ is the injected O_3 mixing ratio at the inlet; τ is the average residence time of the air in the reaction and reference chambers. The relationship between $J(O^1D)$ and γ is shown in Fig. S18, the obtained γ-$J(O^1D)$ equation was used to correct $d[O_3]$ in both chambers during the daytime, thereby eliminating the influence of light-enhanced loss. Our previous study has shown that after this correction, $d[O_3]$ showed no clear correlation with RH for either chamber (Hao et al., 2023), indicating that RH did not affect the O_3 mixing ratio during the observation period. When quantifying $d[O_3]$ from ambient air measurements, we first calculate γ from the measured $J(O^1D)$ using the γ -$J(O^1D)$ equations listed in Fig. S17 for each chamber, then compute $d[O_3]$ from the measured $[O_3]$ and Eq. (S3).

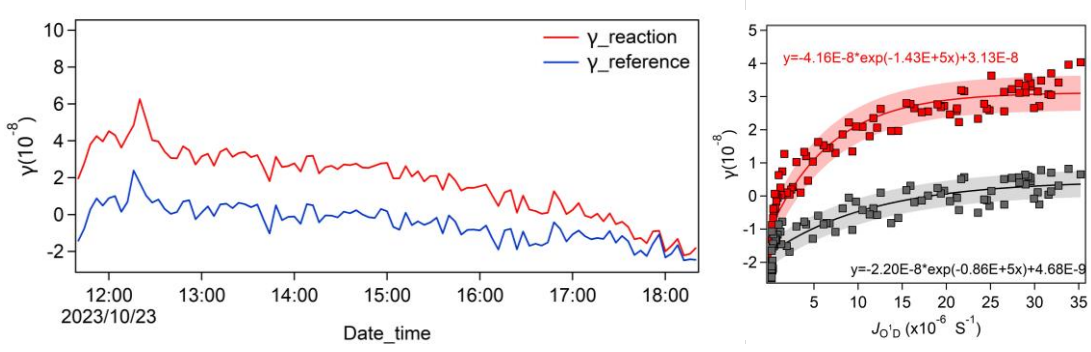

Figure S17: The relationship between γ and $J(O^1D)$ in the reaction and reference chambers, the shaded areas represent the maximum range of fluctuation under this confidence level.

When injecting ambient air into the NPOPR system, the error of $P(O_3)_{net}$ with a residence time of τ can be calculated using Eq. (S4):

$$P(O_3)_{net\_error}=\frac{\sqrt{(O_{X_\gamma})_{rea\_error}^{2}+((9.72\times[O_X]_{rea\_measured}^{-1.0024})_{rea\_std})^{2}+(O_{X_\gamma})_{ref\_error}^{2}+((9.72\times[O_X]_{ref\_measured}^{-1.0024})_{ref\_std})^{2}}}{\tau} \quad (S4)$$

where $(O_{X_\gamma})_{rea\_error}$ and $(O_{X_\gamma})_{ref\_error}$ represent the measurement error due to light-enhanced loss of O_3 in the reaction and reference chambers, respectively, and $(9.72\times[O_X]_{measured}^{-1.0024})_{rea\_std}$ and $(9.72\times[O_X]_{measured}^{-1.0024})_{ref\_std}$ represent the standard deviation of O_X in the reaction and reference chambers, respectively, caused by the CAPS NO_2 monitor with an integration time period of 100 s. Combined with the associated residence time $\langle\tau\rangle$ under different flow rates, i.e., $\langle\tau\rangle$ was 0.16 h at a flow rate of 2.1 L min^{-1}. In our previous research (Hao et al., 2023), we evaluated the residence time error and determined it to be approximately 0.0015, when we considered this error in the calculation of '$P(O_3)_{net}$_error', we observed a minimal reduction in the '$P(O_3)_{net}$_error' values, ranging from 0 to 4% [0.25-0.75 percentile]. This impact is considered negligible in relation to the overall '$P(O_3)_{net}$_error' as presented in Eq. S4. Consequently, we did not consider the uncertainty associated with the residence time in our calculations. We note that this collective measurement error of $P(O_3)_{net}$ is referred to as the measurement precision of the NPOPR detection system, which is different with the measurement accuracy of the NPOPR detection system described above.

S2. HONO measurement and its corresponding error

In this study, the NO_2^- values measured by 2060 Marga M were used as HONO values for model input. During the observation period, the daytime (6:00–18:00) average of NO_2^- values was 0.5 ± 0.5 ppbv, with a maximum value of 2.8 ppbv. This value is consistent with observations from other studies in China. For example, measurements of HONO in urban Beijing from September 2015 to July 2016 showed that HONO concentrations were highest in autumn at 2.3 ± 1.8 ppbv and lowest in winter at 1.1 ± 0.9 ppbv (Wang et al., 2017). Measurements of HONO at a coastal site in Shenzhen in October 2019 reported a value of 0.7 ± 0.1 ppbv (Zhang et al., 2024). Measurements at a site in the Bohai Sea during the autumn of 2018 showed an average HONO concentration of 0.2 ± 0.2 ppbv, with a maximum value of 1.4 ppbv (Wen et al., 2019). However, previous studies have shown the HONO may be overestimated by MARGA due to aqueous phase formation of HONO from dissolved NO_2 and SO_2 at wetted denuder walls (Stieger et al., 2018; Spindler et al. 2003). The measurement error of HONO by MARGA was evaluated by Xu et al. (2019) and Spindler et al. (2003). In this study, we used the method proposed by Spindler et al. (2003) to evaluate measurement uncertainty of HONO database obtained by MARGA, and then checked its influence to the modelled $P(O_3)_{net}$. The overall artefact formation measurement error of HONO by MARGA is expressed as a sum in Eq. (S5):

$$[HNO_2]_{art} = 0.056[NO_2] + (0.0032/ppb)\,[NO_2][SO_2] \quad (S5)$$

where 0.0032 is the reciprocal value of the slope of the straight line between the HNO_2 concentration corrected for the HNO_2 content in purified air, the mean NO_2 artefact and the concentration product of NO_2 and SO_2. We further modelled $P(Ox)_{net}$_Case D_4 with the corrected HONO, and found that the corrected HONO could decrease the modelled $P(Ox)_{net}$_Case D_4 by 0-8%, as shown in Fig. S18. Therefore, we note that with the measurement error of HONO by MARGA, the modelling method may consistently underestimate the modelled $P(Ox)_{net}$ in all cases, and the $P(Ox)_{net}$_missing in our study should be regarded as the lower limit values.

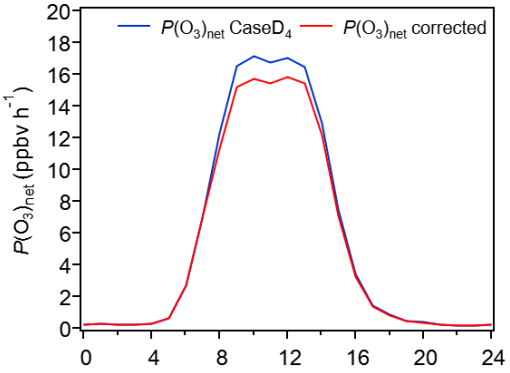

Figure S18: The modelled $P(Ox)_{net}$_Case D_4 with and without the HONO correction.

S3. Heterogeneous reactions of HO_2 and N_2O_5 in the MCM v3.3.1 model

The non-homogeneous loss rates (k) of HO_2 and N_2O_5 on aerosol surfaces are calculated using a simple approach based on first-order loss at the aerosol surface. The loss rate is calculated as follows:

$$k = \frac{\omega \cdot r_x \cdot S_a}{4} \quad (S6)$$

$$S_a = \pi \int_0^\infty D_p^2 n_N(D_p) dD_p = \int_0^\infty n_s(D_p) dD_p \quad (S7)$$

The molecular average velocity ω (m s^{-1}) is calculated using the formula: $\omega = \frac{\sqrt{8RT}}{\pi M}$ where R is the universal gas constant, T is the temperature, and M is the molecular weight of the gas. r_x represents the adsorption coefficient for HO_2 or N_2O_5, which in this study is based on the results from (Zhou et al., 2021), where γ_{HO2} =0.19. S_a represents the aerosol surface area（$m^2\ m^{-3}$）, $n_N(D_p)$ is the particle number concentration, and D_p is the particle diameter. Since the NPOPR sampler removes particles with diameters > 2 μm, only particles with diameters < 2 μm are considered in the model simulation for aerosol surface area.

Cl· is an important oxidant. A modeling study (Sarwar et al., 2014) demonstrated that incorporating Cl· chemistry into models can increase the oxidative capacity of VOCs by more than 20 % in some regions. In the troposphere, one major source of Cl· is the photolysis of nitryl chloride ($ClNO_2$), which is formed from the heterogeneous reaction of N_2O_5 with chloride particles at night.

$$N_2O_5(g) + Cl^-(aq) \rightarrow \varphi ClNO_2(g) + (2-\varphi)NO_3^- \quad \text{(RS1)}$$

$$ClNO_2 \xrightarrow{jClNO_2} Cl\cdot + NO_2 \quad \text{(RS2)}$$

In the equation, φ represents the yield of $ClNO_2$, which is based on the intermediate yield of $ClNO_2$ ($\varphi ClNO_2 = 0.6$) used in Xue et al. (2014) study.

S4. Modelling scenarios of Case A–D1

Based on our previous study(Zhou et al., 2024a), this simulation adopted the same modelling scenarios (Case$A–D_1$) and further explored methods to compensate for the $P(O_3)_{net_}$Missing (see Table S3). The simulation results indicate that compared to Case A, Case B (which incorporated the HO_2 heterogeneous uptake mechanism) showed a 7.6 % decrease in simulated HO_2 concentration (Figure S7 (d)), with a corresponding decrease of 0.6 ppbv h^{-1} (Figure S7 (b),～4.9 %) in averaged daytime $P(O_3)_{net_}$Mod. Case C (which included dry deposition of trace gases and N_2O_5 uptake) resulted in only 0.1 ppbv h^{-1} (～1.1 %) in $P(O_3)_{net_}$Mod compared to Case A. Case D_1 (which added the $ClNO_2$ photolysis mechanism) exhibited negligible impact (～0.0 ppbv h^{-1}), indicating that dry deposition and Cl· chemistry had a minimal impact on $P(O_3)_{net_}$Mod in this study.

S5. Impacts of OVOCs constraints in the model

To explore the impact of OVOCs constraint in the model, we further added a modelling scenario without OVOC constraints based on Case D1 and output key OVOC species (see Fig. S19). From Fig. S19, the model tends to overestimate some OVOC concentrations (i.e., HCHO, CH_3CHO), and their secondary-formation pathways are adequately captured, while the observed diurnal variation of CH_3COCH_3 does not exhibit clear secondary formation characteristics. These results show that directly constraining OVOC concentrations can fill the concentration gap in the model to match observed OVOC levels, but may mask deficiencies in the model's chemical mechanism and artificially suppress diagnostic signals of missing secondary formation pathways (i.e., the RO_2-to-OVOC reaction pathways). This will lead to the underestimation of the entire HOx-cycle oxidation rate, lowers the budgets of OH, O_3, and NO_3, and subsequently the $P(O_3)_{net_}$Mod. However, without any constraint, the model may overestimate the contribution from primary sources. Furthermore, our analysis indicates that the $P(O_3)_{net}$ missing is not likely caused by unaccounted secondary production (see Sect. 3.3). Until such mechanistic gaps are resolved, observational nudging of OVOCs remains a pragmatic compromise: it preserves concentration accuracy while curbing spurious chemical feedbacks.

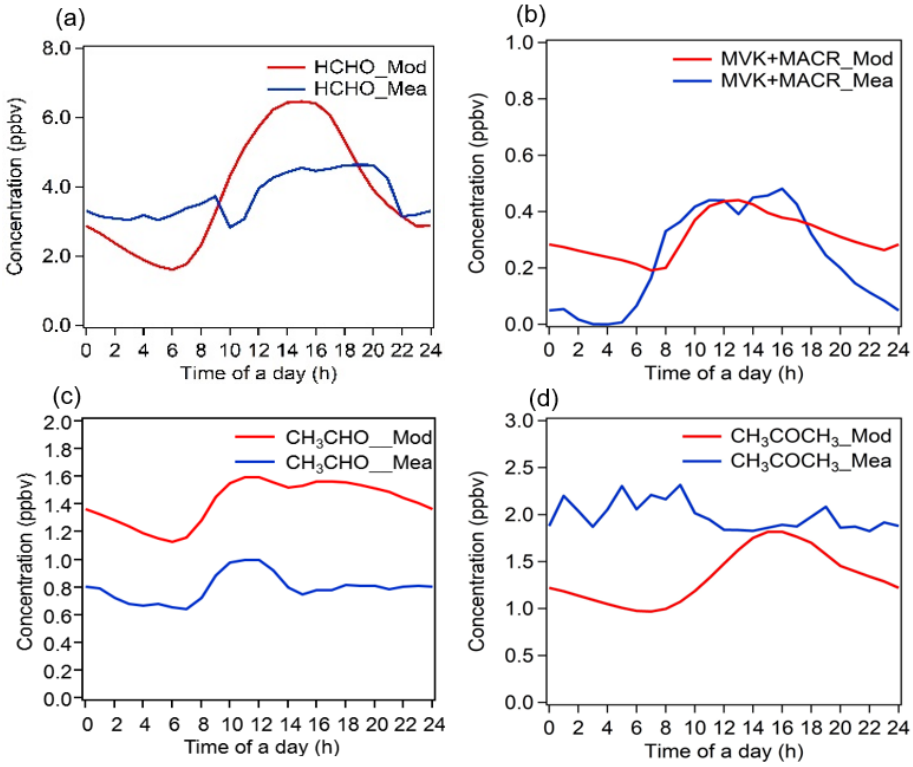

Figure S19: Comparison of measured OVOCs with modeled values from a no-constraint OVOC scenario based on Case D1.

S6. Chemcal budgets of OH and HO_2

The chemical budget of OH and HO_2 can be analyzed using the OBM model outputs, which detail their generation and consumption pathways. According to the overview by Hao et al. (2023), the budget analysis of the production and consumption pathways for OH and HO_2 was conducted using the following equations:

$$P(\mathrm{OH}) = 2\,k_{O(^1D)+H_2O}[O(^1D)][H_2O] + k_{NO+HO_2}[NO][HO_2] + j_{HONO}[HONO] \quad (S8)$$

$$D(\mathrm{OH}) = k_{OH+NO_2}[OH][NO_2] + k_{OH+NO}[OH][NO] + k_{OH+CO}[OH][CO] + \sum_i k_{VOCs_i+OH}[VOCs_i][OH]\varphi_i \quad (S9)$$

$$P(\mathrm{OH})_{net} = P(\mathrm{OH}) - D(\mathrm{OH}) \quad (S10)$$

$$P(\mathrm{HO_2}) = \sum_i k_{VOCs_i+NO_3}[VOCs_i][NO_3]\varphi_i + \sum_i k_{VOCs_i+OH}[VOCs_i][OH]\varphi_i + \sum_i j_{VOCs_i}[OVOCs_i] + k_{OH+CO}[OH][CO] \quad (S11)$$

$$D(\mathrm{HO_2}) = k_{HO_2+NO}[HO_2][NO] \quad (S12)$$

$$P(HO_2)_{net} = P(HO_2) - D(HO_2) \quad (S13)$$

Table S1. Measurement details for different parameters at Guangdong Atmospheric Supersite of China.

Parameters	Instrument Name	Country of manufacture	Instrument Model
$PM_{2.5}$	Fengyue Aorui, $PM_{2.5}$ monitor	China	Fengyue Aorui-AR1000
O_3	Fengyue Aorui, Ozone analyzer	China	Fengyue Aorui-1016
NO/NO_2	Fengyue Aorui, Nitrogen oxides Analyzer	China	Fengyue Aorui-1014
SO_2	Fengyue Aorui, Sulfur dioxide Analyzer	China	Fengyue Aorui-1032
CO	Fengyue Aorui, Carbon monoxide Analyzer	China	Fengyue Aorui-1012
Photolysis rates	Metcon, actinic flux spectrometer	Germany	j_{NO_2}-j_{O_3}
Particle size distribution	Particle size spectrometer	China	TSI-3321, 3775, 3776
VOCs	Peng Yu Chang Ya, Online VOCs Monitor	China	ZF-PKU-VOC1007/PTR-TOF-1000
HCHO	SDL Technology, Formaldehyde analyzer	China	Model 4050
NO_2^-(HONO)	Mereohm Applikon	Switzerland	2060 Marga M

Note: The actinic flux spectrometer measures eight types of photolysis rates (j_{NO_2}, j_{O^1D}, j_{HONO}, $j_{H_2O_2}$, $j_{NO_3\_M}$, $j_{NO_3\_R}$, j_{HCHO_M}, and j_{HCHO_R}). Detailed information on the calibration and quality assurance of these instruments can be found in a previous study (Yan et al., 2022).

Table S2. List of photolysis rates obtained from direct measurements and the TUV Model.

Species	Source	Species	Source
j_{O^1D}	Measured	j_{MEK}	TUV
j_{O_3}	TUV	j_{MVK}	TUV
$j_{H_2O_2}$	Measured	j_{GLYOX_1}	TUV
j_{NO_2}	Measured	j_{GLYOX_2}	TUV
$j_{NO_3\_1}$	Measured	j_{GLYOX_3}	TUV
$j_{NO_3\_2}$	Measured	j_{MGLYOX}	TUV
j_{HONO}	Measured	j_{BIACET}	TUV
j_{HNO_3}	TUV	j_{CH_3OOH}	TUV
j_{HCHO_1}	Measured	$j_{CH_3NO_3}$	TUV
j_{HCHO_2}	Measured	$j_{C_2H_5NO_3}$	TUV
j_{CH_3CHO}	TUV	$j_{NC_3H_7NO_3}$	TUV
$j_{C_2H_5CHO}$	TUV	$j_{TC_4H_9NO_3}$	TUV
j_{MACR}	TUV	j_{NOA}	TUV
$j_{CH_3COCH_3}$	TUV	j_{CLNO_2}	TUV

Note: The photolysis rates obtained from the TUV model were corrected for cloud shading scenarios by comparing the measured j_{NO_2} with the j_{NO_2} obtained from the TUV model.

Table S3. Description of different modelling scenarios and the parameter settings

Case	Description	Parameter settings	references
A	Ambient gases (NO, NO_2, SO_2, CO, O_3), HONO, 44 VOCs, meteorological parameters (*T*, RH, *P*, BLH), photolysis rates, and O_3 dry deposition	O_3（0.27 cm s^{-1}）	(Xue et al., 2014)
B	Case A with the addition of HO_2 uptake	γ_{HO2}=0.19	(Zhu et al., 2020; Zhou et al., 2021)
C	Case B with the addition of trace gases (NO_2, SO_2, H_2O_2, HNO_3, PAN, HCHO) dry deposition	NO_2（0.6 cm s^{-1}） SO_2（0.8 cm s^{-1}） H_2O_2（1.2 cm s^{-1}） HNO_3（4.7 cm s^{-1}） PAN（0.4 cm s^{-1}） HCHO（0.9 cm s^{-1}）	(Zhang et al., 2003; Xue et al., 2014)
D_1	Case C with the addition of N_2O_5 non-homogeneous absorption reactions and $ClNO_2$ photolysis	γ_{N2O5}=0.02 φ_{ClNO_2} =0.6	(Xue et al., 2014; Badger et al., 2006; Xia et al., 2019; Xia et al., 2020)
D_2	Case D_1 with increased constraints for acetaldehyde, acrolein, acetone, and butanone	Constraints based on measurement data	——
D_3	Case D_1 with increased constraints for all measurable OVOCs		——
D_4	Case D_3 with increased constraints for all measurable chlorinated VOCs		——
E_1	Case D_1 with overall VOCs concentration in constraints increased	Increase based on the correlation between $P(O_3)_{net}$_Missing and k_{OH}_Missing	——
E_2	Case D_1 with increased concentrations of ethylene and formaldehyde in constraints		——
E_3	Case D_1 with increased formaldehyde concentration in constraints		——

Notes: Parameter values for modelling scenarios from Case A to Case D_1 are set the same as those in Zhou et al. (2024a).

Table S4. Measured VOCs concentrations during the observation periods at Guangdong Atmospheric Supersite of China (units: μg m^{-3}).

Chemicals	Classification	Mean±SD (μg m^{-3})	Chemicals	Classification	Mean±SD (μg m^{-3})
Acetylene		0.1±0.1	Tetrahydrofuran*	OVOCs	0.9±0.8
Acetylene	NMHC/ AVOCs	0.1±0.1	tert-Butyl methyl ether	OVOCs	0.0±0.0
Alkanes		2.6±1.6	Acetic acid**	OVOCs	21.4±9.0
Ethane	NMHC/ AVOCs	0.3±0.1	Methanol**	OVOCs	12.5±4.4
Propane	NMHC/ AVOCs	0.4±0.3	Formic acid**	OVOCs	8.7±2.3
Isobutane	NMHC/ AVOCs	0.3±0.4	Methyl vinyl ketone**	OVOCs	0.5±0.3
n-Butane	NMHC/ AVOCs	0.1±0.2	Aromatics		2.7±1.8
Cyclopentane*	NMHC/ AVOCs	0.1±0.2	Toluene	NMHC/ AVOCs	1.1±0.9
2-Methylbutane	NMHC/ AVOCs	0.2±0.3	Benzene	NMHC/ AVOCs	0.1±0.0
Pentane	NMHC/ AVOCs	0.1±0.2	Ethylbenzene	NMHC/ AVOCs	0.2±0.2
Cyclohexane	NMHC/ AVOCs	0.0±0.1	o-Xylene	NMHC/ AVOCs	0.2±0.2
2,2-Dimethylbutane	NMHC/ AVOCs	0.0±0.0	Cumene	NMHC/ AVOCs	0.0±0.0
2,3-Dimethylbutane	NMHC/ AVOCs	0.1±0.1	N-Propylbenzene	NMHC/ AVOCs	0.0±0.0
2-Methylpentane	NMHC/ AVOCs	0.1±0.1	2-Ethyltoluene	NMHC/ AVOCs	0.0±0.0
3- Methylpentane	NMHC/ AVOCs	0.1±0.1	3-Ethyltoluene	NMHC/ AVOCs	0.0±0.0
Hexane	NMHC/ AVOCs	0.1±0.1	Mesitylene	NMHC/ AVOCs	0.0±0.0
Methylcyclohexane*	NMHC/ AVOCs	0.0±0.0	4-Ethyltoluene	NMHC/ AVOCs	0.0±0.0
2,4-Dimethylpentane*	NMHC/ AVOCs	0.0±0.0	1,2,4-Trimethylbenzene	NMHC/ AVOCs	0.1±0.1
2-Methylhexane	NMHC/ AVOCs	0.1±0.1	1,2,3-Trimethylbenzene	NMHC/ AVOCs	0.0±0.0
3-Methylhexane	NMHC/ AVOCs	0.1±0.1	1,3-Diethylbenzene*	NMHC/ AVOCs	0.0±0.0
Heptane	NMHC/ AVOCs	0.1±0.1	1,4- Diethylbenzene*	NMHC/ AVOCs	0.0±0.0
2,2,4-Trimethylpentane*	NMHC/ AVOCs	0.0±0.0	P/m-Xylene	NMHC/ AVOCs	0.6±0.5
2,3,4- Trimethylpentane*	NMHC/ AVOCs	0.0±0.0	Styrene	NMHC/ AVOCs	0.1±0.2
2-Methylheptane*	NMHC/ AVOCs	0.0±0.0	Naphthalene*	NMHC/ AVOCs	0.1±0.1
3- Methylheptane*	NMHC/ AVOCs	0.0±0.0	Halocarbons		3.0±1.7
n-Octane	NMHC/ AVOCs	0.0±0.0	Chloromethane	AVOCs	0.1±0.0
n-Nonane	NMHC/ AVOCs	0.0±0.0	Dichloromethane	AVOCs	1.3±0.9
Decane	NMHC/ AVOCs	0.0±0.0	Chloroform	AVOCs	0.1±0.0
n-Hendecane	NMHC/ AVOCs	0.2±0.1	Methyl bromide	AVOCs	0.0±0.0

2,3-Dimethylpentane*	NMHC/ AVOCs	0.0±0.0	Bromodichloromethane*	AVOCs	0.0±0.0
Alkenes		0.2±0.3	Dichlorodifluoromethane*	AVOCs	0.6±1.3
Ethylene	NMHC/ AVOCs	0.1±0.1	Bromoform*	AVOCs	0.0±0.0
Propylene	NMHC/ AVOCs	0.0±0.0	Chlorodibromomethane*	AVOCs	0.0±0.0
1-Butene	NMHC/ AVOCs	0.0±0.0	Trichlorofluoromethane*	AVOCs	0.1±0.0
cis-2-Butene*	NMHC/ AVOCs	0.1±0.2	Chloroethane	AVOCs	0.0±0.0
2- Butene*	NMHC/ AVOCs	0.0±0.0	1,1-Dichloroethane	AVOCs	0.0±0.0
Isoprene	BVOCs	0.0±0.0	1,2-Dichloroethane	AVOCs	0.2±0.1
1-Pentene	NMHC/ AVOCs	0.0±0.0	1,2-Dibromoethane	AVOCs	0.0±0.0
trans-2-Pentene	NMHC/ AVOCs	0.0±0.0	1,2-DichlorotetrafluoroethaneI	AVOCs	0.0±0.0
cis-2-Pentene	NMHC/ AVOCs	0.0±0.0	1,1,2,2-Tetrachloroethane*	AVOCs	0.0±0.0
1-Hexene	NMHC/ AVOCs	0.0±0.0	Magnesia mixture*	AVOCs	0.1±0.0
1,3-Butadiene	NMHC/ AVOCs	0.0±0.0	1,1,1-Trichloroethane	AVOCs	0.0±0.0
OVOCs		5.7±2.9	1,1,2-Trichloroethane	AVOCs	0.0±0.0
Formaldehyde	OVOCs	0.5±0.3	1,2-Dichloropropane	AVOCs	0.1±0.1
Acetaldehyde	OVOCs	0.1±0.1	Vinyl chloride	AVOCs	0.0±0.0
Propionaldehyde	OVOCs	0.0±0.0	Vinyldene chloride	AVOCs	0.0±0.0
Butyraldehyde	OVOCs	0.0±0.0	trans-1,2-Dichloroethylene	AVOCs	0.0±0.0
Valeraldehyde	OVOCs	0.0±0.1	cis-1,2-Dichloroethylene	AVOCs	0.0±0.0
Hexanal	OVOCs	0.6±0.5	Phenyl vinyl sulfone*	AVOCs	0.0±0.0
Acrolein	OVOCs	0.0±0.0	Trichloroethylene	AVOCs	0.0±0.0
Crotonaldehyde	OVOCs	0.2±0.0	Tetrachloroethylene	AVOCs	0.1±0.0
Methacrolein	OVOCs	0.0±0.0	Hexachloro-1,3-butadiene*	AVOCs	0.1±0.1
Benzaldehyde	OVOCs	0.0±0.1	Chlorobenzene*	AVOCs	0.0±0.0
Acetone	OVOCs	0.5±0.3	1,2-Dichlorobenzene*	AVOCs	0.0±0.0
2-Butanone	OVOCs	0.3±0.3	1,3-Dichlorobenzene*	AVOCs	0.0±0.0
4-Methyl-2-pentanone	OVOCs	0.0±0.0	1,4-Dichlorobenzene*	AVOCs	0.0±0.0
2-Hexanone	OVOCs	1.3±1.3	1,2,4-Trichlorobenzene*	AVOCs	0.1±0.1
1,4-Dioxane*	OVOCs	0.0±0.0	Carbon tetrachloride*	AVOCs	0.1±0.0
Vinyl acetate*	OVOCs	0.0±0.0	Other		0.0±0.0
Ethyl acetate Methyl	OVOCs	1.2±0.8	Carbon disulfide*	AVOCs	0.0±0.0
Methacrylate*	OVOCs	0.0±0.0	Dimethyl sulfide**	AVOCs	0.8±0.1

Note: VOC species not labeled in the table are measured by ZF-PKU-VOC1007 and are included in the observation data analysis;

VOC species labeled with "**" are measured by PTR-TOF-1000, but these are not included in the total sum as they serve as supplementary inputs for the model; VOC species labeled with "*" are not included in the MCM v3.3.1 chemical mechanism.

Table S5. The daytime average and standard deviation of pollutants and meteorological parameters during O_3 pollution days and normal days throughout the observation period (from October 4 to 26, 2023).

Parameter	Entire observation period	O_3 pollution days	Normal days
j_{NO_2} ($\times 10^{-3}$ s^{-1})	3.1±2.6	3.7±2.6	2.7±2.5
T (℃)	28.1±4.5	32.0±3.5	31.5±5.1
RH (%)	64.9±16.6	55.5±11.2	63.2±14.4
NO (ppbv)	3.1±4.2	4.3±6.4	2.6±3.0
NO_2 (ppbv)	13.4±6.0	15.4±8.0	12.8±5.0
O_3 (ppbv)	39.8±31.3	63.2±37.6	30.9±22.9
TVOCs (μg m^{-3})	13.2±7.1	13.8±8.4	13.1±6.7
$P(O_3)_{net}$ (ppbv h^{-1})	9.7±7.4	14.4±13.8	7.1±9.4
CO (ppmv)	0.6±0.1	0.5±0.1	0.6±0.10
$PM_{2.5}$ (μg m^{-3})	28.1±13.4	41.0±10.9	23.4±11.3
Wind speed (m s^{-1})	3.4±1.5	2.5±1.2	3.8±1.3
Wind direction (°)	80.7±110.1	76.1±52.9	80.8±125.5

Table S6. Maximum measured $P(O_3)_{net}$ values based on dual-reaction chamber technique in literatures.

Measurement site	Site type	Study period	$P(O_3)_{net}$（ppbv h^{-1}）	References
USA - Houston	Urban	April-May 2009	100	(Cazorla et al., 2012)
USA - Bloomington	Suburban	May 2010	~30	(Sklaveniti et al., 2018)
USA - Houston	Urban	September-October 2013	40~50	(Baier et al., 2015)
USA - Golden	Urban	Summer 2014	~30	(Baier et al., 2017)
Japan - Kosakakuri	Forest	August 2014	10.5	(Sadanaga et al., 2017)
China - Lhasa	Urban	June 2021	30.9	(Chen et al., 2024)
China - Beijing	Urban	June 2021	42.7	(Chen et al., 2024)
China - Shenzhen	Urban	December 2021	34.1	(Hao et al., 2023)
China - Hefei	Suburban	September-October 2022	27.8	(Tong et al., 2025)
China - Dongguan	Urban	March 2023	46.3	(Zhou et al., 2024b)
China - Jiangmen	Rural	October 2023	53.7	This study

Table S7. The daytime mean of $P(O_3)_{net}$ in all modelling scenarios, their simulation deviations, and the IOA between the $P(O_3)_{net}$_Mea and $P(O_3)_{net}$_Mod.

Modelling cases	Daytime mean $P(O_3)_{net}$ (ppbv h^{-1})	Relative deviation* (%)	IOA_1	IOA_2	R	MB (ppbv h^{-1})	NMB (%)	RMSE (ppbv h^{-1})	MFB (%)	MFE (%)
Measured	13.0±9.8	——	——	——	——	——	——	——	——	——
A	10.4±6.6	20.3	0.66	0.87	0.98	-2.4	-24.9	7.0	-3.1	53.8
B	9.7±6.2	25.2	0.66	0.86	0.84	-2.9	-29.4	7.2	-1.7	55.0
C	9.6±6.2	26.3	0.66	0.86	0.84	-3.0	-30.5	7.2	-1.7	55.5
D_1	9.6±6.2	26.3	0.66	0.86	0.84	-3.0	-30.5	7.2	-1.7	55.5
D_2	9.56±6.1	26.6	0.66	0.86	0.85	-3.0	-30.5	7.2	-12.6	55.6
D_3	10.0±6.2	23.0	0.66	0.87	0.84	-2.6	-26.1	7.0	-9.9	52.9
D_4	10.1±6.3	22.2	0.66	0.87	0.84	-2.5	-25.3	7.0	-8.9	52.6
E_1	11.7±7.5	10.3	0.64	0.92	0.72	-1.4	-8.9	6.1	4.1	25.4
E_2	10.8±6.9	17.2	0.64	0.89	0.71	-2.2	-14.8	6.7	-4.1	26.9
E_3	12.4±8.0	5.1	0.64	0.92	0.72	-0.7	-4.4	6.1	8.8	25.5

Notes: *Calculated from the following equation: $\frac{P(O_3)_{net}\_missing}{P(O_3)_{net}\_mea} \times 100\%$; IOA_1 represents the Index of Agreement for O_3, while the other evaluation metrics (IOA_2, R, MB, NMB, RMSE, MFB, MFE) are used to assess $P(O_3)_{net}$. The mean $P(O_3)_{net}$ values for both $P(O_3)_{net}$_Mea and $P(O_3)_{net}$_Mod excluding rainy days.

Overall, Case E_1–E_3 significantly improve the simulation accuracy of $P(O_3)_{net}$ and reduce simulation bias by optimizing model mechanisms, particularly in terms of MB, NMB, and RMSE. Although the R slightly decreases, the overall simulation performance is superior to other scenarios.

Table S8. List of input VOC species for the different modelling scenarios

Species	Name in MCM Mechanism	Constrained Scenarios	Species	Name in MCM Mechanism	Constrained Scenarios
Acetylene	C2H2	All Cases	4-Methyl-2-pentanone	MIBK	Case D_3, D_4
Ethane	C2H6	All Cases	2-Hexanone	HEX2ONE	Case D_3, D_4
Propane	C3H8	All Cases	Methyl tert-butyl ether	MTBE	Case D_3, D_4
Isobutane	IC4H10	All Cases	Toluene	TOLUENE	All Cases
n-Butane	NC4H10	All Cases	Benzene	BENZENE	All Cases
Isopentane	IC5H12	All Cases	Ethylbenzene	EBENZ	All Cases
Pentane	NC5H12	All Cases	o-Xylene	OXYL	All Cases
Cyclohexane	CHEX	All Cases	Cumene	IPBENZ	All Cases
2,2-Dimethylbutane	M22C4	All Cases	n-Propylbenzene	PBENZ	All Cases
2,3-Dimethylbutane	M23C4	All Cases	1-Ethyl-2-methylbenzene	OETHTOL	All Cases
2-Methylpentane	M2PE	All Cases	1-Ethyl-3-methylbenzene	METHTOL	All Cases
3-Methylpentane	M3PE	All Cases	1,3,5-Trimethylbenzene	TM135B	All Cases
Hexane	NC6H14	All Cases	4-Ethyltoluene	PETHTOL	All Cases
2-Methylhexane	M2HEX	All Cases	1,2,4-Trimethylbenzene	TM124B	All Cases
3-Methylhexane	M3HEX	All Cases	1,2,3-Trimethylbenzene	TM123B	All Cases
Heptane	NC7H16	All Cases	p/m-Xylene	PXYL/MXYL	All Cases
n-Octane	NC8H18	All Cases	Styrene	STYRENE	Case D_3, D_4
n-Nonane	NC9H20	All Cases	Chloromethane	CH3CL	Case D_4
Decane	NC10H22	All Cases	Dichloromethane	CH2CL2	Case D_4
n-Hendecane	NC11H24	All Cases	Chloroform	CHCL3	Case D_4
Ethylene	C2H4	All Cases	Methyl bromide	CH3BR	Case D_4
Propylene	C3H6	All Cases	Chloroethane	CH3CH2CL	Case D_4
1-Butene	BUT1ENE	All Cases	1,1-Dichloroethane	CHCL2CH3	Case D_4
Isoprene	C5H8	All Cases	1,2-Dichloroethane	CH2CLCH2CL	Case D_4
1-Pentene	PENT1ENE	All Cases	1,2-Dibromoethane	DIBRET	Case D_4
trans-2-Pentene	TPENT2ENE	All Cases	1,1,2,2-Tetrachloroethane	CHCL2CHCL2	Case D_4
cis-2-Pentene	CPENT2ENE	All Cases	1,1,1-Trichloroethane	CH3CCL3	Case D_4
1-Hexene	HEX1ENE	All Cases	1,1,2-Trichloroethane	CH2CLCHCL2	Case D_4
1,3-Butadiene	C4H6	All Cases	1,2-Dichloropropane	CL12PROP	Case D_4

Formaldehyde	HCHO	All Cases	Vinyl chloride	VINCL	Case D_4
Acetaldehyde	CH3CHO	Case D_2, D_3, D_4	1,1-Dichloroethylene	CCL2CH2	Case D_4
Propionaldehyde	C2H5CHO	Case D_3, D_4	trans-1,2-Dichloroethylene	TDICLETH	Case D_4
Butyraldehyde	C3H7CHO	Case D_3, D_4	cis-1,2-Dichloroethylene	CDICLETH	Case D_4
Valeraldehyde	C4H9CHO	Case D_3, D_4	Trichloroethylene	TRICLETH	Case D_4
Hexanal	C5H11CHO	Case D_3, D_4	Tetrachloroethylene	TCE	Case D_4
Acrolein	ACR	Case D_2, D_3, D_4	Acetic acid	CH3CO2H	Case D_3, D_4
Crotonaldehyde	C4ALDB	Case D_3, D_4	Methanol	CH3OH	Case D_3, D_4
Methacrolein	MACR	Case D_3, D_4	Formic acid	HCOOH	Case D_3, D_4
Benzaldehyde	BENZAL	Case D_3, D_4	Methyl vinyl ketone	MVK	Case D_3, D_4
Acetone	CH3COCH3	Case D_2, D_3, D_4	Dimethyl sulfide	DMS	Case D_3, D_4
2-Butanone	MEK	Case D_2, D_3, D_4	Ethyl acetate	ETHACET	Case D_3, D_4

References

Badger, C. L., Griffiths, P. T., George, I., Abbatt, J. P., and Cox, R. A.: Reactive uptake of N_2O_5 by aerosol particles containing mixtures of humic acid and ammonium sulfate, The Journal of Physical Chemistry A, 110, 6986-6994, doi:10.1021/jp0562678, 2006.

Baier, B. C., Brune, W. H., Lefer, B. L., Miller, D. O., and Martins, D. K.: Direct ozone production rate measurements and their use in assessing ozone source and receptor regions for Houston in 2013, Atmospheric Environment, 114, 83-91, doi:10.1016/j.atmosenv.2015.05.033, 2015.

Baier, B. C., Brune, W. H., Miller, D. O., Blake, D., Long, R., Wisthaler, A., Cantrell, C., Fried, A., Heikes, B., and Brown, S.: Higher measured than modeled ozone production at increased NO_X levels in the Colorado Front Range, Atmospheric Chemistry and Physics, 17, 11273-11292, doi:10.5194/acp-17-11273-2017, 2017.

Cazorla, M., Brune, W., Ren, X., and Lefer, B.: Direct measurement of ozone production rates in Houston in 2009 and comparison with two estimation methods, Atmospheric Chemistry and Physics, 12, 1203-1212, doi:10.5194/acp-12-1203-2012, 2012.

Chen, Y., Chi, S., Wang, Y., Guo, S., Zhang, C., Ye, C., and Lin, W.: Ozone production sensitivity in the highland city of Lhasa: a comparative analysis with Beijing, Air Quality, Atmosphere & Health, 1-11,http://doi.org/10.1007/s11869-024-01604-4, 2024.

Hao, Y., Zhou, J., Zhou, J.-P., Wang, Y., Yang, S., Huangfu, Y., Li, X.-B., Zhang, C., Liu, A., and Wu, Y.: Measuring and

modeling investigation of the net photochemical ozone production rate via an improved dual-channel reaction chamber technique, Atmospheric Chemistry and Physics, 23, 9891-9910, doi:10.5194/acp-23-9891-2023, 2023.

Sadanaga, Y., Kawasaki, S., Tanaka, Y., Kajii, Y., and Bandow, H.: New system for measuring the photochemical ozone production rate in the atmosphere, Environmental science & technology, 51, 2871-2878, doi:10.1021/acs.est.6b04639, 2017.

Sarwar, G., Simon, H., Xing, J., and Mathur, R.: Importance of tropospheric $ClNO_2$ chemistry across the Northern Hemisphere, Geophysical Research Letters, 41, 4050-4058, doi:10.1002/2014GL059962, 2014.

Sklaveniti, S., Locoge, N., Stevens, P. S., Wood, E., Kundu, S., and Dusanter, S.: Development of an instrument for direct ozone production rate measurements: Measurement reliability and current limitations, Atmospheric Measurement Techniques, 11, 741-761, doi:10.1029/98jd00349, 2018.

Spindler, G., Hesper, J., Brüggemann, E., Dubois, R., Müller, T., and Herrmann, H.: Wet annular denuder measurements of nitrous acid: laboratory study of the artefact reaction of NO_2 with S(IV) in aqueous solution and comparison with field measurements: Atmospheric Environment, 37, 2643, doi:10.1016/S1352.2310(03)00209.7, 2003.

Stieger, B., Spindler, G., Fahlbusch, B., Müller, K., Grüner, A., Poulain, L., Thöni, L., Seitler, E., Wallasch, M., and Herrmann, H.: Measurements of PM_{10} ions and trace gases with the online system MARGA at the research station Melpitz in Germany – A five-year study, Journal of Atmospheric Chemistry, 75, 33–70, doi.org/10.1007/s10874-017-9361-0, 2018.

Tong, J., Hu, R., Hu, C., Liu, X., Cai, H., Lin, C., Zhong, L., Wang, J., and Xie, P.: Development of a net ozone production rate detection system based on dual-channel cavity ring-down spectroscopy, Journal of Environmental Sciences, 149, 419-430, doi:10.1016/j.jes.2024.01.035, 2025.

Wang, J., Zhang, X., Guo, J., Wang, Z., and Zhang, M.: Observation of nitrous acid (HONO) in Beijing, China: Seasonal variation, nocturnal formation and daytime budget, Science of the Total Environment, 587, 350-359, doi:10.1016/j.scitotenv.2017.02.159, 2017.

Xu, Z., Liu, Y., Nie, W., Sun, P., Chi, X., and Ding, A.: Evaluating the measurement interference of wet rotating-denuder–ion chromatography in measuring atmospheric HONO in a highly polluted area: Atmospheric Measurement Techniques, 12, 6737–6748, doi:/10.5194/amt.12.6737, 2019.

Wen, L., Chen, T., Zheng, P., Wu, L., Wang, X., Mellouki, A., Xue, L., and Wang, W.: Nitrous acid in marine boundary layer over eastern Bohai Sea, China: Characteristics, sources, and implications, Science of the total environment, 670, 282-291, doi:10.1016/j.scitotenv.2019.03.225, 2019.

Xia, M., Peng, X., Wang, W., Yu, C., Sun, P., Li, Y., Liu, Y., Xu, Z., Wang, Z., and Xu, Z.: Significant production of $ClNO_2$ and possible source of Cl_2 from N_2O_5 uptake at a suburban site in eastern China, Atmospheric Chemistry and Physics, 20, 6147-6158, doi:10.5194/egusphere-egu2020-12946, 2020.

Xia, M., Wang, W., Wang, Z., Gao, J., Li, H., Liang, Y., Yu, C., Zhang, Y., Wang, P., and Zhang, Y.: Heterogeneous uptake of N_2O_5 in sand dust and urban aerosols observed during the dry season in Beijing, Atmosphere, 10, 204, doi:10.3390/atmos10040204, 2019.

Xue, L., Wang, T., Gao, J., Ding, A., Zhou, X., Blake, D., Wang, X., Saunders, S., Fan, S., and Zuo, H.: Ground-level ozone

in four Chinese cities: precursors, regional transport and heterogeneous processes, Atmospheric Chemistry and Physics, 14, 13175-13188, doi:10.5194/acp-14-13175-2014, 2014.

Yan, Z., Tao, Z., Yujun, L., Duohong, C., and Chengliu, L.: The characteristics and source of formaldehyde in the Pearl River Delta and its impact on ozone formation, Environmental Chemistry, 41, 2356-2363, doi: 10.7524/j.issn.0254-6108.2021112906, 2022.

Zhang, G., Hu, R., Xie, P., Hu, C., Liu, X., Zhong, L., Cai, H., Zhu, B., Xia, S., and Huang, X.: Intensive photochemical oxidation in the marine atmosphere: evidence from direct radical measurements, Atmospheric Chemistry and Physics, 24, 1825-1839, doi:10.5194/acp-24-1825-2024, 2024.

Zhang, L., Brook, J. R., and Vet, R.: A revised parameterization for gaseous dry deposition in air-quality models, Atmospheric Chemistry and Physics, 3, 2067-2082, doi:10.5194/acp-3-2067-2003, 2003.

Zhou, J., Sato, K., Bai, Y., Fukusaki, Y., Kousa, Y., Ramasamy, S., Takami, A., Yoshino, A., Nakayama, T., and Sadanaga, Y.: Kinetics and impacting factors of HO_2 uptake onto submicron atmospheric aerosols during the 2019 Air QUAlity Study (AQUAS) in Yokohama, Japan, Atmospheric Chemistry and Physics, 21, 12243-12260, doi:10.5194/acp-21-12243-2021, 2021.

Zhou, J., Wang, W., Wang, Y., Zhou, Z., Lv, X., Zhong, M., Zhong, B., Deng, M., Jiang, B., and Luo, J.: Intercomparison of measured and modelled photochemical ozone production rates: Suggestion of chemistry hypothesis regarding unmeasured VOCs, Science of The Total Environment, 951, 175290, doi:10.1016/j.scitotenv.2024.175290, 2024a.

Zhou, J., Wang, W., Wang, Y., Zhou, Z., Lv, X., Zhong, M., Zhong, B., Deng, M., Jiang, B., Luo, J., Cai, J., Li, X.-B., Yuan, B., and Shao, M.: Intercomparison of measured and modelled photochemical ozone production rates: Suggestion of chemistry hypothesis regarding unmeasured VOCs, Science of The Total Environment, 951, 175290, doi:/10.1016/j.scitotenv.2024.175290, 2024b.

Zhu, J., Cheng, H., Peng, J., Zeng, P., Wang, Z., Lyu, X., and Guo, H.: O_3 photochemistry on O_3 episode days and non-O_3 episode days in Wuhan, Central China, Atmospheric Environment, 223, 117236, doi:10.1016/j.atmosenv.2019.117236, 2020.